Somatosensory, Light-Driven, Thin-Film Robots Capable of Integrated Perception and Motility

Xiao-Qiao Wang, Kwok Hoe Chan, Yin Cheng, Tianpeng Ding, Tongtao Li, Sippanat Achavananthadith, Selman Ahmet, John S. Ho, and Ghim Wei Ho*

Living organisms are capable of sensing and responding to their environment through reflex-driven pathways. The grand challenge for mimicking such natural intelligence in miniature robots lies in achieving highly integrated body functionality, actuation, and sensing mechanisms. Here, somatosensory light-driven robots (SLiRs) based on a smart thin-film composite tightly integrating actuation and multisensing are presented. The SLiR subsumes pyro/piezoelectric responses and piezoresistive strain sensation under a photoactuator transducer, enabling simultaneous yet non-interfering perception of its body temperature and actuation deformation states. The compact thin film, when combined with kirigami, facilitates rapid customization of low-profile structures for morphable, mobile, and multiple robotic functionality. For example, an SLiR walker can move forward on different surfaces, while providing feedback on its detailed locomotive gaits and subtle terrain textures, and an SLiR anthropomorphic hand shows bodily senses arising from concerted mechanoreception, thermoreception, proprioception, and photoreception. Untethered operation with an SLiR centipede is also demonstrated, which can execute distinct, localized body functions from directional motility, multisensing, to wireless human and environment interactions. This SLiR, which is capable of integrated perception and motility, offers new opportunities for developing diverse intelligent behaviors in soft robots.

Biological systems have long been a source of inspiration for the design of more capable robots.[1–3] In order to adapt to changing environments, living organisms can actively sense and respond to physical cues.[4,5] Mimicking such intelligent responses in artificial systems is a long-standing challenge that requires the integration of stimulus-responsive motility and perception feedback in a robotic body.[6] To date, the mainstream efforts on robot intelligence have been made in programmable control of rigid bodies that rely on individual computational modeling and electric actuation to achieve specific prescribed robot actions,[7] while the complex computing systems, power sources, and electrical motors restrict the robot body from size miniaturization and high-level of motion adaptivity. The realization of intelligent response in a miniature robot requires new design strategies capable of providing tightly coupled actuation and sensing mechanisms, and body compliance.

Soft robotics is an emerging field that strives to bridge the gap between robots and biological living organisms.[8] Unlike conventional hard machines, soft robots are comprised of structures that continuously response, deform and morph in efforts to autonomously adapt to surroundings, manipulate objects, and execute dexterous maneuvers.[9] Without doubt, the stimulus responsiveness and multifunctionalities of active soft matter have opened up opportunities for diverse designs of actuation strategies[10–15] (including light, heat, humidity, electrical, pneumatic, and magnetic actuation) and sensing schemes[16–20] (such as resistive, capacitive, and self-powered sensing). Synchronous motility and multisensory perception in one compact system, especially when the robot size is down to centimeter scale, still proves a particular fabrication challenge.[21] So far, limited embodiments based on a single mode of sensory feedback mechanism have been achieved,[22–29] such as ionic capacitive sensors embedded in a pneumatic actuator,[23] liquid metal strain sensors integrated in a soft gripper,[30] and piezoresistive strain feedback in artificial muscles.[26] And few attempts at integrating multifunctional sensing schemes[31,32] have revealed inherent limitations in multiple connection terminals, complex electric power inputs, and complicated fabrication processes, where trade-offs between the actuation/shape adaptivity and sensing capability is unavoidable.

Here, we overcome these challenges using an integral thin-film construct to demonstrate fabrication of customizable,

Dr. X.-Q. Wang, K. H. Chan, Dr. Y. Cheng, Dr. T. Ding, Dr. T. Li,
S. Achavananthadith, S. Ahmet, Prof. J. S. Ho, Prof. G. W. Ho
Department of Electrical and Computer Engineering
National University of Singapore
4 Engineering Drive 3, Singapore 117583, Singapore
E-mail: elehgw@nus.edu.sg
Prof. G. W. Ho
Institute of Materials Research and Engineering
A*STAR (Agency for Science, Technology, and Research)
3 Research Link, Singapore 117602, Singapore
Prof. G. W. Ho
Materials Science and Engineering
National University of Singapore
9 Engineering Drive 1, Singapore 117575, Singapore

The ORCID identification number(s) for the author(s) of this article can be found under https://doi.org/10.1002/adma.202000351.

**ADVANCED
SCIENCE NEWS**

www.advancedsciencenews.com

**ADVANCED
MATERIALS**

www.advmat.de

miniature soft robots capable of simultaneous perception and motility. The thin-film monolithically integrates arbitrarily patternable sensors and actuators and can be readily transformed into a 3D robot through kirigami techniques. The result is a somatosensory, light-driven robot that subsumes coordinated actuation, proprio-exteroception and communication capabilities. These material sets and integration strategies enable the following advances: i) synchronous and non-interfering sensation of strain and temperature enabled by two separate electric signals, together with uninterrupted photothermal actuation; ii) real-time feedback of walking gaits, and assessment of terrain textures; iii) customizable soft robot architectures and functionalities via combinatorial thin-film kirigami; iv) biomimetic untethered robot prototypes with built-in actuation-sensing specific responses, showing distributed body deformations, collective mobility, and wireless perception of the surroundings.

The composite thin-film structures and working mechanisms of somatosensory, light-driven robots (SLiRs) are presented in **Figure 1**. Specifically, three core active materials integrated in the thin film are ferroelectric poly(vinylidene difluoride) (PVDF), photothermal polydopamine reduced graphene oxide (PDG) and conductive graphite–carbon nanotube composites (graphite–CNT) (middle of Figure 1a). As schematically shown, the PDG and PVDF layer with opposite coefficient of thermal expansion (CTE) constitute a bimorph actuator that is not only heat responsive, but also light responsive, given

that the PDG is able to absorb and convert light into heat,[33] thereby enabling light actuation. The cross-sectional SEM image presents a compact lamellar microstructure of the PDG nanosheets (bottom right of Figure 1a). In addition, all trans β-phase arrangement of polymer chain produces permanent dipoles in PVDF,[34] the orientation change of dipoles in response to temperature variation generates a pyroelectric potential across the thickness direction of the PVDF, and thus built-in temperature detection ability based on a self-powered pyroelectric scheme (bottom left of Figure 1a). The top layer is a U-shaped graphite–CNT circuit, forming a compliant strain sensor along PVDF film, and SEM images in Figure S1, Supporting Information, show uniform surface morphology of the composite graphite–CNT on PVDF. The homogeneous networks of optimized mass ratio of graphite–CNT blend (top right of Figure 1a) realizes precise strain feedback by reducing the resistance response to photothermal effect to bare minimum. When SLiR is light actuated, it bends convex upward, resulting in a stretched conductive circuit. This in turn causes resistance increase, thereby translating the real-time piezoresistive signal to actuation displacement along the length direction (top left of Figure 1a). 3D printing technique is employed to lay down selective circuity on the body parts of SLiR (Figure 1b). Notably, the conductive graphite–CNT circuit and PDG on the opposite sides of PVDF can act as two electrodes to collect photothermal pyroelectric voltage signals, and thus only three lightweight
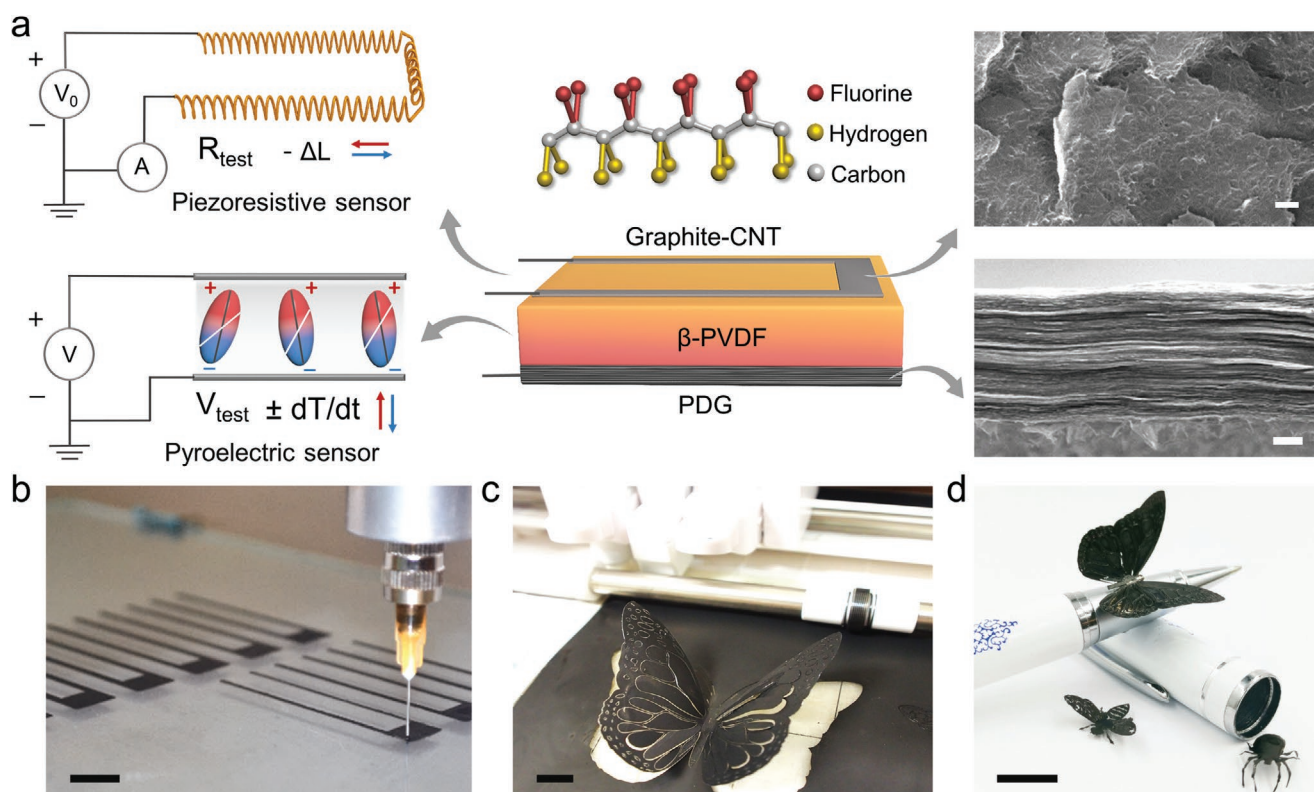

Figure 1. The structure–function design of SLiR. a) Materials system and microstructure of SLiR, and working mechanisms of the pyroelectric temperature and piezoresistive strain perception. Scale bar (top), 500 nm. Scale bar (bottom), 3 µm. b) 3D printing for a planar array of graphite–CNT strain sensors on a PVDF film. c) Programmable cutting of a kirigami butterfly SLiR robot from the thin-film construct. d) Mini SLiR robots. Scale bars, 1 cm.
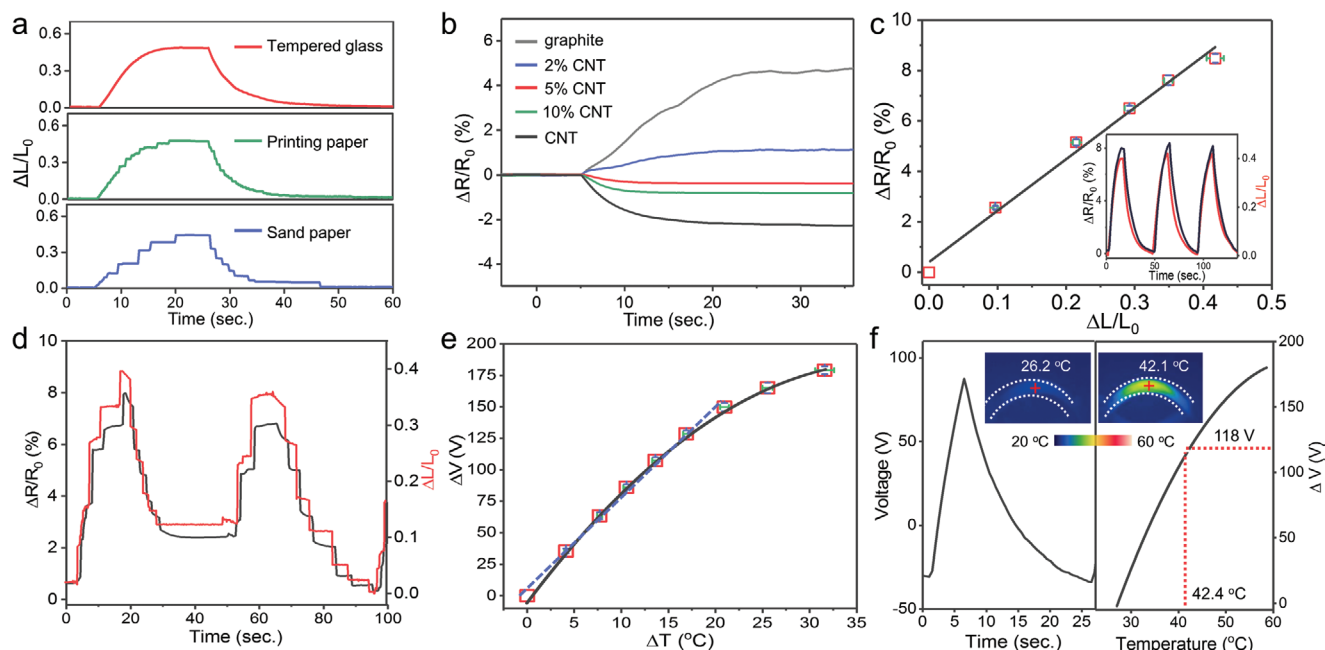
**ADVANCED
SCIENCE NEWS**

www.advancedsciencenews.com

**ADVANCED
MATERIALS**

www.advmat.de

Figure 2. Realization of accurate deformation and temperature feedback. a) Time-dependent photothermal actuation deformation on different surfaces. b) Relative change of resistance of the graphite/PVDF, CNT/PVDF, and hybrid graphite–CNT/PVDF films under light illumination. c) Relative change of resistance as a function of photothermal actuation deformation on the tempered glass. The inset shows the time-dependent resistance change and actuation deformation under photothermal actuation cycles. d) Time-dependent resistance change and actuation deformation of SLiR working on the sand paper. e) The change of open circuit voltage as a function of photothermal temperature change. f) Time-dependent open circuit voltage upon a 5-s light pulse and the measure temperature of SLiR calculated through the curve of voltage change as a function of temperature. The inset infrared images show the real temperature change.

carbon fiber electrode connections are adopted in the actuation and sensing system. Meanwhile, the kirigami technique allows one-step programmable customization of diverse robot prototypes (Figure 1c), and we were able to fabricate miniature SLiR robots with sizes down to millimeter scale, such as the mini robot bee and spider (Figure 1d). Based on our described geometry design and multifunctionality of the materials, photothermal actuation and dual-parameter sensations can be compactly integrated into the thin-film device. In doing so, the temperature variation and actuation strain are respectively detected via the embodied pyroelectricity of PVDF and piezoresistivity of graphite–CNT circuit, facilitating simultaneous and decoupled read-out signals.

We first actuated the SLiR film (50 × 10 mm) and measured its photothermal and mechanical actuation on different surfaces. Figure S2, Supporting Information, shows the actuation scheme, dimension, and resistance (≈20 kΩ) of the U-shaped graphite–CNT circuit. Under a visible light illumination of 100 mW cm^{-2}, the flat SLiR film continuously bends convex upward due to the photo-thermomechanical conversion (Figure S3, Supporting Information). Besides, the actuation stress generated by the SLiR film were evaluated (Figure S4, Supporting Information). Near infrared light can also trigger the actuation owing to high light absorption of PDG in the visible and near infrared regions (Figure S5, Supporting Information). Particularly, due to the distinct interaction with the surface textures, SLiRs can have different actuation deformation characteristics on different substrates. The actuation deformation $\Delta L/L_0$ is defined here as the tip displacement ΔL divided

by the original length L_0 of SLiR film, and we tracked the moving end of SLiR (Figure S6, Supporting Information) and plotted the time-dependent actuation deformation in **Figure 2**a. The maximum actuation deformation on the tempered glass, printing paper and sand paper are 0.490, 0.472, and 0.443, respectively. Moreover, compared to a smooth moving trajectory on the tempered glass, the actuation deformation-release path on the printing paper shows numerous small random steps, while the sand paper shows fewer and larger trajectory steps. Due to the coupled thermomechanical behavior, realization of precise feedback of the actuation motions on different surfaces necessitates sensitive strain detection that is isolated from the influence of temperature fluctuations.

To track the actuation deformation process of SLiR on different surfaces, photothermal temperature interference to the piezoresistive sensor is eliminated and piezoresistivity in the three-layer material system is emphasized. It is known that the resistance of a graphite or CNT film changes with temperature, which is unavoidable owing to its inherent thermoresistivity (i.e., temperature dependence of the resistance). Nevertheless, by utilizing the opposite temperature coefficient of resistance (TCR) of metallic graphite and semi-conductive CNT, we were able to downplay the photothermal temperature and resistance association.[35] The photothermal resistive behaviors of graphite, CNT, and graphite–CNT hybrid films were evaluated (Figure 2b). Notably, the large effect of photothermal expansion of PVDF on the resistance of the conductive films must be taken into consideration. Hence all the optimizations were conducted on PVDF, and meanwhile the bilayer

ADVANCED
SCIENCE NEWS

www.advancedsciencenews.com

ADVANCED
MATERIALS

www.advmat.de

graphite–CNT/PVDF films were mechanically constrained during the light heating process, allowing accurate assessment of the thermoresistive behavior in the absence of actuation deformation. With photothermal temperature rising to the maximum ≈65 °C, the relative resistance change $\Delta R/R_0$ of graphite and CNT film are 4.8% and −2.3%, respectively. Significantly, the hybridization diminishes temperature dependency of the resistance, and $\Delta R/R_0$ of hybrid films with an optimized mass ratio of CNTs to graphite at 5% is only −0.3%, achieving a temperature self-compensation outcome. After that, the introduction of PDG layer enables the PVDF/PDG bimorph actuator driven by light. The theoretical calculation of curvature of the bimorph as a function of PDG thickness was conducted based on the classical Timoshenko beam theory, which agrees well with the experimental results (Figures S7–S9, Supporting Information), and PDG thickness of 15 µm is chosen for further studies (Figure S10, Supporting Information). Besides, the presence of PDG layer makes considerable enhancement of the piezoresistivity, which is essential to achieve sensitive perception of subtle actuation deformation. Under a fixed bending deformation at 0.5, relative resistance change of the strain sensor increases from 2.5% to 9.5% when the PDG thickness increases from 0 to 15 µm (Figure S11, Supporting Information). Stability of the piezoresistivity is further demonstrated by measuring resistance response of the SLiR film to cyclic bending deformation at different levels and loading speeds (Figures S12 and S13, Supporting Information).

Then we started to evaluate the actuation deformation feedback capability of SLiR. Inset of Figure 2c depicts time-dependent deformation trajectory of SLiR on the tempered glass under repeated light pulses and concurrent resistance changes of its strain sensor (Movie S1, Supporting Information). As illustrated, the resistance change follows the deformation during each of the repeated actuation cycles. In this respect, SLiR exhibits 8.5% resistance change for around actuation deformation at 0.417. Additionally, the photothermal resistance change is further confirmed to have a negligible effect on the accuracy of deformation perception (see details in Figure S14, Supporting Information). $\Delta R/R_0$ is able to continuously follow the actuation deformation trajectory when exposed to a long-time light illumination (Figure S15, Supporting Information). Moreover, we recorded the maximum actuation deformation and resistance change under different light pulses (Figure S16, Supporting Information), and it is derived that the relative resistance change is almost linearly correlated to the actuation deformation of SLiR (Figure 2c), allowing easy assessment of actuation state using $\Delta R/R_0$. SLiR film was further subjected to repeated light pulses (8/22 s on/off cycle) over 5 h, and no decline in sensing performance is observed (Figure S17, Supporting Information). Furthermore, the time-dependent resistance change waveforms correspond well with the stepwise actuation deformation paths on the sand paper or printing paper (Figure 2d; Figure S18 and Movie S2, Supporting Information), suggesting that we have realized precise and sensitive feedback of actuation deformation states.

Temperature perception constitutes another important element of somatosensory feedback, especially for a robot that is driven by heat. According to the pyroelectric theory, the open

circuit voltage V between the top and bottom electrodes of PVDF film can be expressed by

$$V = \frac{pd}{\varepsilon_{33}^T}\Delta T \tag{1}$$

where ε_{33}^T is the relative permittivity of PVDF, p is the pyroelectric coefficient, d is the thickness of PVDF, and ΔT is the change of temperature.[36,37] When SLiR is exposed to light pulse, the photothermal temperature change is detected via the output voltage. Movie S3, Supporting Information, shows that the change of voltage can synchronously follow the temperature oscillations of SLiR under repeated light pulses, exhibiting a favorable slow-adaptive sensing mode. Considering all pyroelectric materials are piezoelectric,[38] the temperature perception via pyroelectricity might be principally interrupted by the actuation deformation. However, in our case of photothermal actuation, the piezoelectric output voltage generated by the actuation deformation is substantially smaller compared to the photothermal pyroelectric voltage (Figure S19, Supporting Information). Hence, the actuation deformation has a negligible effect on the pyroelectric voltage. The temperature and voltage waveforms correspond well during each of the light pulses (Figure S20, Supporting Information). In particular, the output current matches well with the rate of temperature change (dT/dt), demonstrating a typical characteristic of pyroelectricity (Figure S21, Supporting Information). The voltage change, ΔV as a function of the temperature change, ΔT (ambient temperature ≈26 °C) is plotted in Figure 2e. Notably, a linear ΔV–ΔT relationship can be clearly seen within a temperature change of 20 °C. As such, a ΔT of 4 °C induced by a 1 s light pulse tallies with a ΔV of 34.6 V, indicating a sensitive pyroelectric temperature detection, that is, equivalent to a sensitivity of ≈8.7 V °C⁻¹. As an additional control experiment, SLiR was constrained and subjected to a 5-s light pulse, and the infrared image in Figure 2f shows that the real temperature changes from 26.2 to 42.1 °C. In accordance with the ΔV–T calibration curve, the detected ΔV of 118.0 V is expected to comply with a temperature of about 42.4 °C, which does concur. This verifies that the accuracy of pyroelectric temperature perception is independent of the actuation deformation. The output voltage signals are reversible and repeatable across 18 000 cycles of 15-s light pulses separated by 30-s rest periods (Figure S22, Supporting Information). Besides, SLiR can also sense external compressive force via the piezoelectricity when no temperature stimulus is engaged. SLiR exhibits stable piezoelectric voltage responses to horizontal force pulses in the length direction or vertical force pulses along the thickness direction (see details in Figure S23, Supporting Information).

Realization of adaptive locomotion and autonomous information feedback represents a significant step forward in the development of artificial intelligent soft robotics. By virtue of the thin-film feature, we can easily transform repeated actuation of SLiR into directional locomotion via a biomimetic geometry design.[39] Continuous and stable forward locomotion was achieved under repeated light pulses (see details in Figure S24, Supporting Information). During this process, we can track and analyze the walking gaits and physical conditions
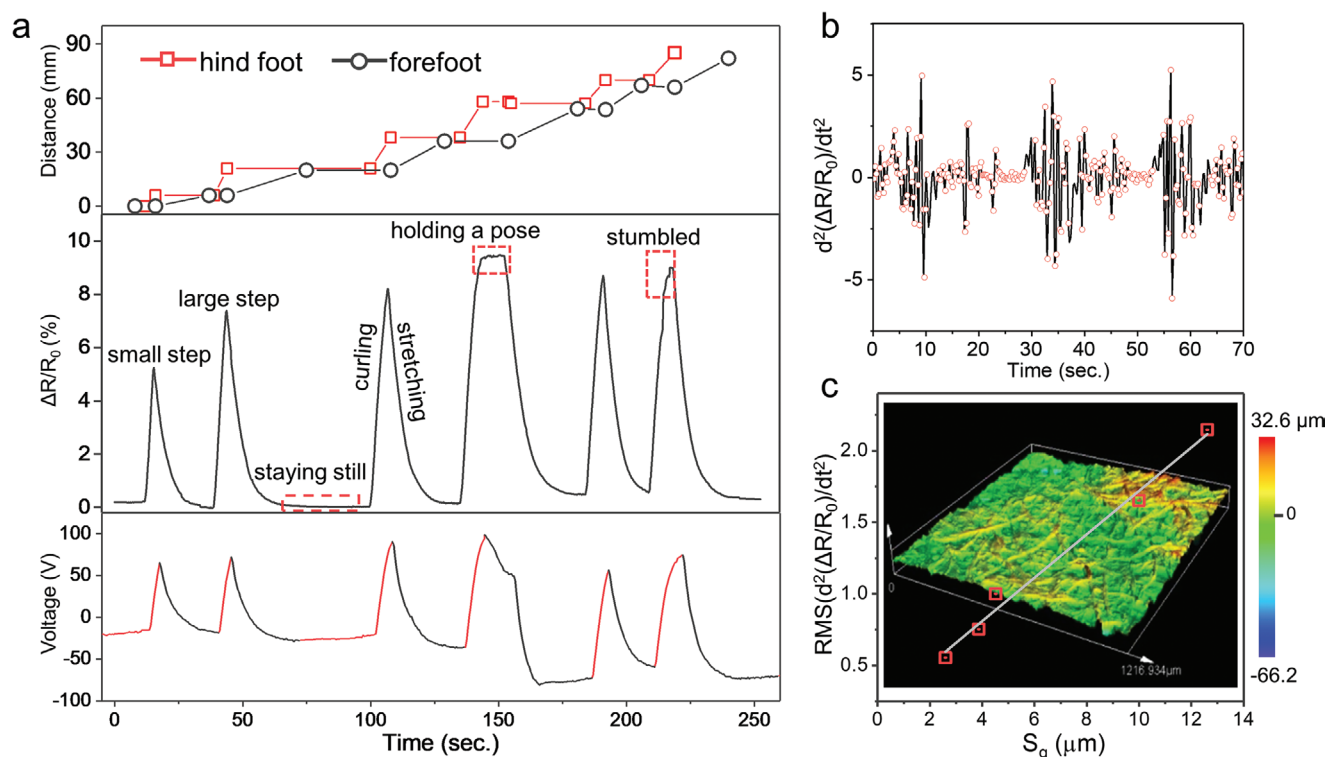
Figure 3. Real-time monitoring of the walking gaits of SLiR and exploration of the surface topography. a) Time-dependent walking gaits, resistance change, and output voltage of SLiR walking forward on the weighing paper (from top to bottom). b) Accelerated rate of the relative change of resistance as a function of time when SLiR walks forward on filter paper. c) RMS value of $d^2(\Delta R/R_0)/dt^2$ as a function of the areal surface roughness of the surface. The inset image is a laser-scanning microscopic image of the filter paper surface.

of the SLiR walker. **Figure 3**a presents time-dependent footsteps of the hind foot and forefoot, resistance change and output voltage (from top to bottom). The waveform of resistance change delivers detail information of the walking gaits. An increase of resistance indicates the body curling via the forward step of hind foot, while a decrease of resistance shows the body stretching using the forefoot. Each of the step length can be evaluated by the value of $\Delta R/R_0$. When $\Delta R/R_0$ is close to zero, the robot is at lying flat position; when $\Delta R/R_0$ is constant at a certain value, the robot is holding a fixed pose. When the robot crosses the joint of two weighing papers, the step-wise change of $\Delta R/R_0$ shows that the robot stumbles and moves forward. Movie S4, Supporting Information, captures the whole perceptive motility process. The output voltage gives us the information of robot body temperature (see details in Table S1, Supporting Information). In addition, the forward locomotion of SLiR is seen to be viable and self-adaptive on different surfaces (Movie S5, Supporting Information). Significantly, by further analyzing the resistance feedback signal, we can acquire the surface roughness. Figure S25, Supporting Information, presents the resistance waveforms of SLiR walking forward on the low to high level roughness surfaces, for example, weighing paper, printing paper, filter paper, and coarse paper, respectively. The 3D laser-scanning microscopic images show corresponding surface textures, and the image data processing gives the areal surface roughness, S_q of 2.6, 3.9, 9.9, and 12.6 µm, respectively. Figure 3b depicts accelerated rate of the relative change of resistance $(d^2(\Delta R/R_0)/dt^2)$ as a function of time on

the filter paper. The calculated root-mean-square (RMS) values of $d^2(\Delta R/R_0)/dt^2$ (Figure S26, Supporting Information) reveal a linear $RMS(d^2(\Delta R/R_0)/dt^2)–S_q$ relationship (Figure 3c). These results attest SLiR adaptive forward locomotions on different surfaces, and capability of assessing the roughness as it threads through different surface topographies.

Complex 3D flexible structures that incorporate active and functional materials are of growing interest for many emerging systems, such as biosensing, energy harvesting, and mechanobiology.[40–42] Here, the robust thin-film SLiR integrating sensors and actuators when combined with the kirigami technique provides new opportunities for advanced soft robotics. **Figure 4**a presents examples of programmed 3D architectures transforming from the corresponding 2D precursors triggered by light, including saddles, nested cage, closed-loop S-shape and star-shape dome. By utilizing our strategy, design of various SLiR robot prototypes is feasible. In addition, the inherent features of compliance and low weight SLiR enable robots to safely interact with humans, especially for functional wearable applications. Kirigami "clothes" with bioinspired scale patterns[43] can conform to a curved scaffold to showcase concepts of thermal regulation and artificial muscle assistance (Figure 4b). The scaly patterns on the "clothes" are able to spontaneously curl in an outward direction to afford openings for heat dissipation when the temperature increases (top of Figure 4b), while frictional anisotropy of the scaly patterns renders assisted movement of the scaffold load under light pulses (bottom of Figure 4b). Besides,
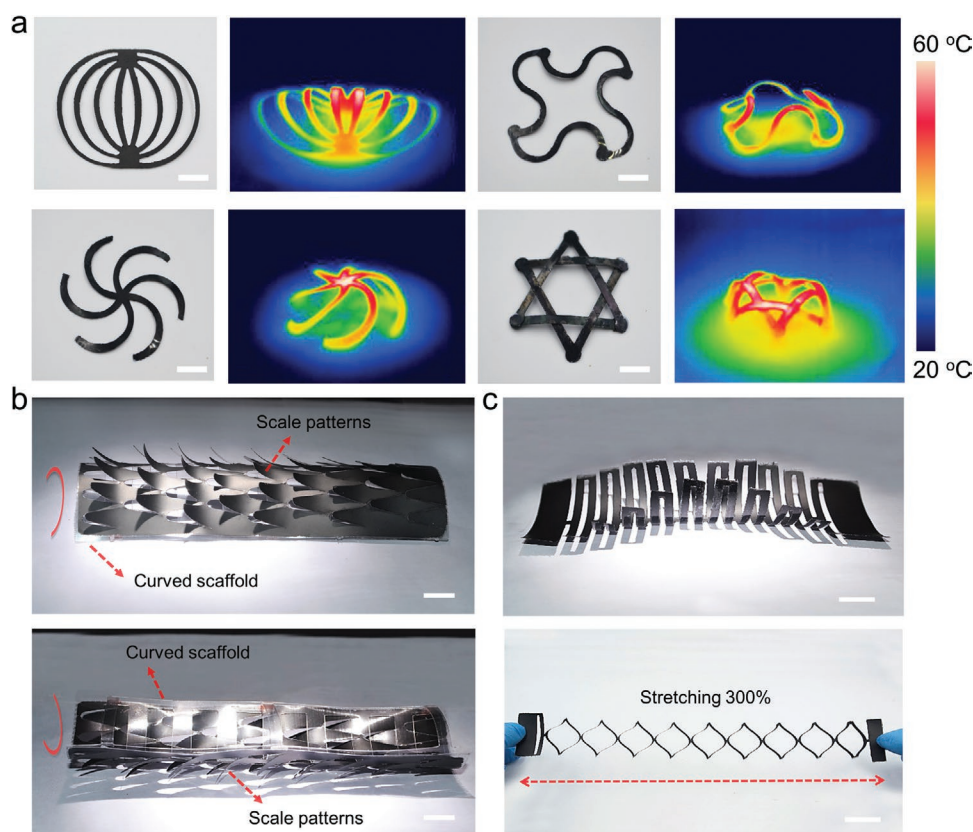
Figure 4. Customizable SLiR robot functionalities. a) Complex photothermal actuated 3D architectures. Scale bars, 1 cm. b) Self-adaptive thermal actuation of the conformable SLiR with bioinspired scaly patterns (top) and walking assistant (bottom). Scale bars, 1 cm. c) Light actuation (top) and stretchability of SLiR (bottom). Scale bar (top), 1 cm. Scale bar (bottom), 3 cm.

a deterministic design via kirigami is utilized to impart stretchability to SLiR, and the film is easily stretched to 300% of its original length (Figure 4c).

To further illustrate the adaptivity of our technique, we fabricated an SLiR anthropomorphic hand with intelligence inspired by a real hand. The five fingers are akin to somatosensory receptors: photoreceptor, mechanoreceptor, thermoreceptor, and proprioceptor, related to the specific stimuli triggered receptor (left of **Figure 5**a). Each of the perceptive fingers can independently bend (right of Figure 5a, part 1 of Movie S6, Supporting Information), and the resistance changes according to the particular finger movements when they repeatedly bend/unbend (Figure 5b). The fingers can also feel an external object temperature. Figure 5c depicts the voltage response of the index finger touching and moving away from a hot cup (≈60 °C) and a cold cup (≈0 °C). In addition, the SLiR hand was demonstrated to distinguish softness/hardness of different objects. We measured the output resistance of the index finger when it bent toward the thumb for a pinching action (part 2 of Movie S6, Supporting Information). Figure 5d shows the photos of free pinching and object (soft sponge) pinching. Correspondingly, $\Delta R/R_0$ constantly increases to ≈3.6% for free bending deformation of the index finger, while $\Delta R/R_0$ is ≈2.6% when the deformation is restricted by the sponge (Figure 5e). Based on the values of $\Delta R/R_0$, we can distinguish the relative softness of the three pinched objects (sponge, ecoflex, and polystyrene

foam with the same size), whereby the sponge is shown to be the softest object.

Furthermore, we devised an untethered SLiR centipede-like prototype, which consists of distinct body parts with disparate functionalities. Light actuated artificial muscles make up the feet of SLiR centipede, facilitating light-driven motility, in conjunction with autonomous perception of temperature and texture as demonstrated (**Figure 6**a), while its antenna is tasked to collect surrounding environment information, and wirelessly transmit data by near-field communication (NFC) device.[44] Directional locomotions can be achieved by light induced reconfiguration in the shape of its body, frictional anisotropy of their feet to propel itself, and control of the PVDF alignment direction[12] while localized light pulse further defines specified locomotion directions. When the alignment was along the width direction of its body, the light pulse to the hind body induced upward bending deformation of its body along the length direction. Meanwhile, the preferred orientation of SLiR feet made sliding in the forward direction much easier than the backward one, and thus the robot could move directionally (Movie S7, Supporting Information). Light pulses to fore body of the centipede with PVDF alignment along the length direction enabled the fore body to move left, while the hind body kept stationary. Hence, the centipede was able to turn around (Movie S8, Supporting Information). Besides, if the light pulse was imposed on the whole body, the centipede crawled
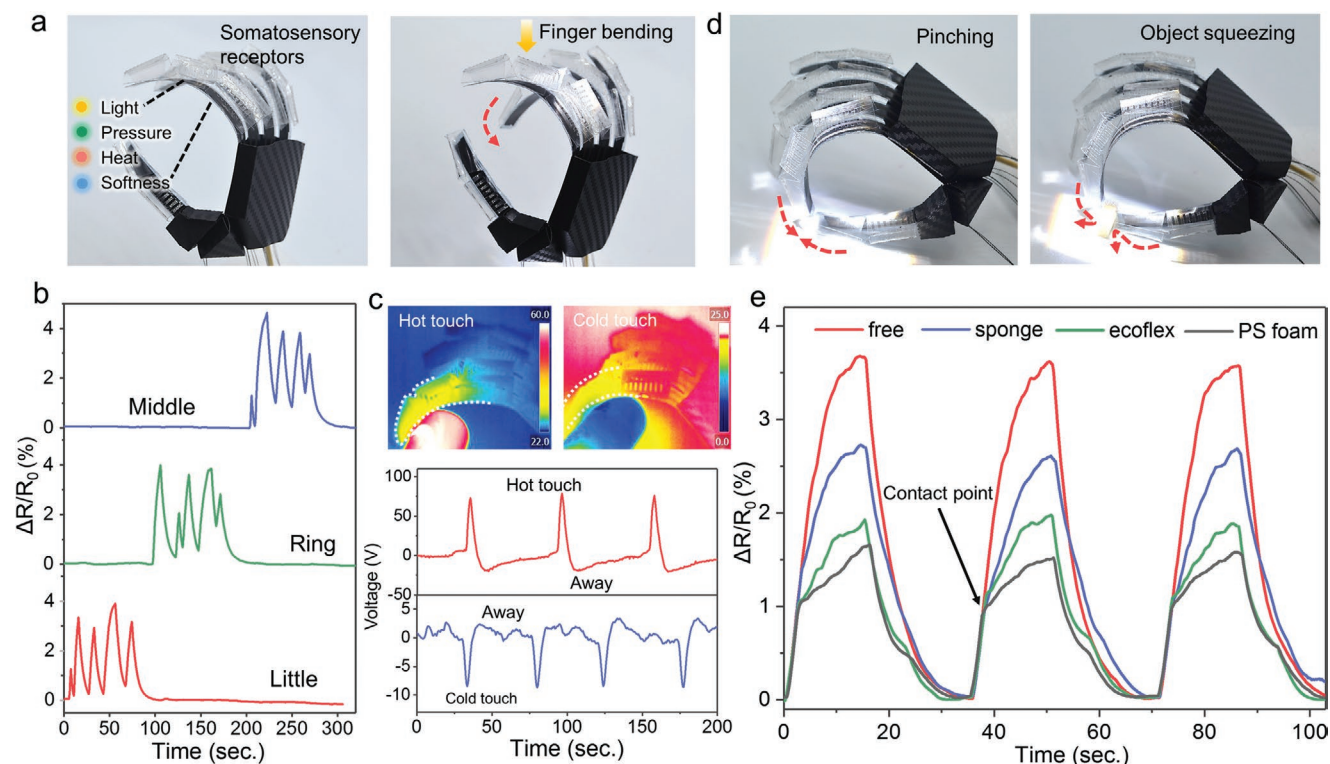
ADVANCED
SCIENCE NEWS
www.advancedsciencenews.com

ADVANCED
MATERIALS
www.advmat.de

Figure 5. SLiR anthropomorphic hand. a) SLiR hand (left) and bending of its middle finger (right). b) Resistance response to each finger movements. c) Voltage response to index finger touching and moving away from a hot cup (≈60 °C) and a cold cup (≈ 0 °C). d) Pinching motion of SLiR hand (left) and squeezing a sponge (right). e) Resistance response of the index finger during free pinching motion and squeezing objects with different softness.
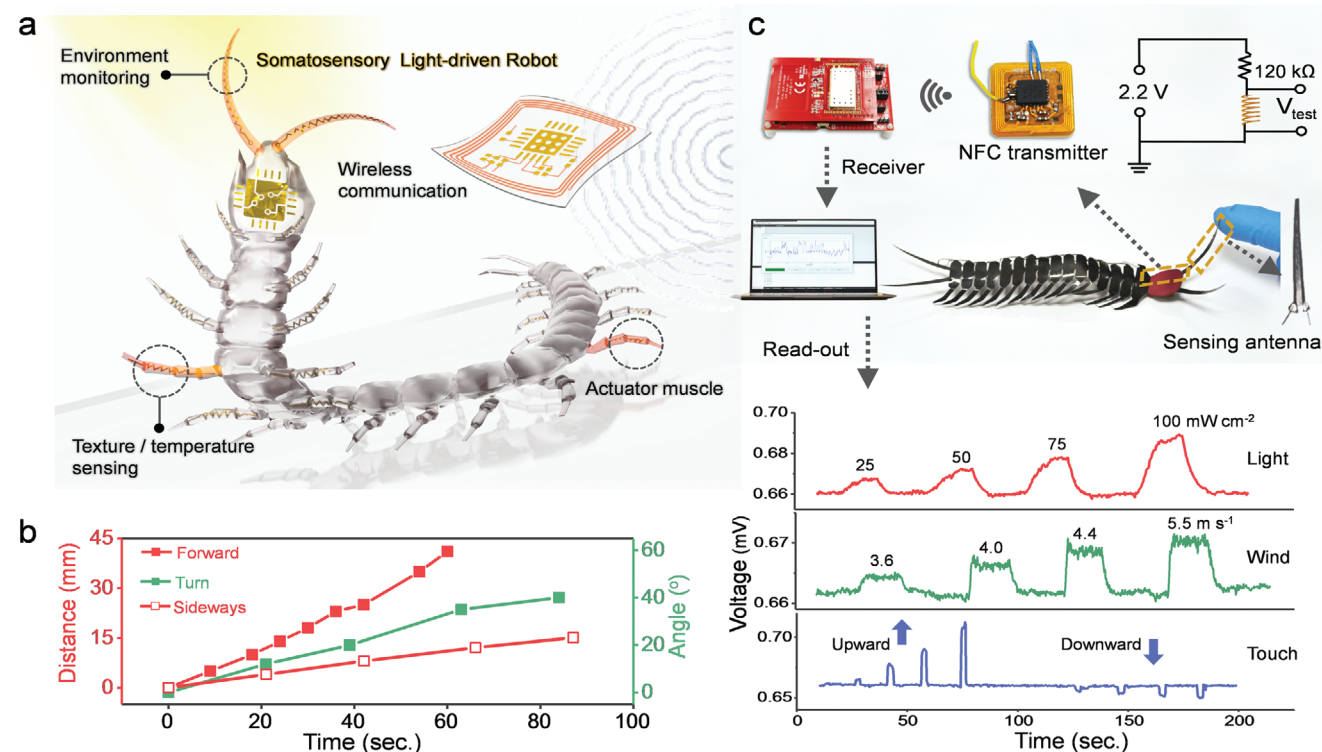

Figure 6. Untethered SLiR centipede. a) Schematic illustration of functionalities of an SLiR centipede. b) Directional locomotion performance of the SLiR centipede including undulating forward, turning, and sideway crawling. c) Wireless antenna sensing of light illumination intensity, wind speed, and touch via NFC.

**ADVANCED
SCIENCE NEWS**

www.advancedsciencenews.com

**ADVANCED
MATERIALS**

www.advmat.de

sideways (Movie S9, Supporting Information). Figure 6b and Figure S27, Supporting Information, show the three kinds of locomotion process enabled by our design principle. To consolidate the diverse locomotion directions unto one centipede, different PVDF alignment directions were further applied to its body parts, and the centipede was able to move forward and turn, respectively (Figure S28 and Movie S10, Supporting Information). The antenna of the centipede was designed to wirelessly interact with the environment and human interventions. Resistance change of the antenna was recorded by the NFC device and wirelessly transmitted to the laptop (Figure 6c), and forward moving motion of SLiR centipede carrying the microchip is shown in Figure S29, Supporting Information. Different visible light illumination intensities and wind speeds ranging from 25 to 100 mW cm^{-2} and 3.5 to 5.5 m s^{-1}, respectively, were recorded, and different finger touching strength in opposite directions can also be differentiated (Movie S11, Supporting Information). Notably, the autonomous response signals to different types of stimulus show identifiable characteristics, in terms of the time-dependent voltage waveforms.

In summary, we have demonstrated SLiRs via seamless integration of multimodal perception and light actuation into monolithic thin-film constructs. The thin-film layup of active materials (conductive graphite–CNT composites, ferroelectric PVDF and photothermal PDG) enables perception of actuation deformation state and body temperature of the robot utilizing respective piezoresistive and pyroelectric effects. Taking advantage of the thin-film integrating sensors and actuators, we are able to custom design kirigami soft robots capable of multitask functions and information feedback. For example, an SLiR walker can spontaneously provide detailed feedback information on its locomotive gaits and body temperatures, and an SLiR anthropomorphic hand possesses alike somatosensory receptions, that is, specific finger movements, hot/cold sensation, and hardness/softness perception. Also, an untethered SLiR centipede is capable of performing walking and turning locomotions, and wireless light intensity, wind speed, and human touch sensing. These coordinated actuation and proprio-exteroception as demonstrated, may inspire diverse designs of intelligent behaviors in soft robots. We expect the SLiR with embedded sensory system to find potential in active human–robot interaction, wearable robot, environmental data collection robot, and closed-loop control of actuation and sensing system.

Experimental Section

Experimental Section is available in Supporting Information.

Supporting Information

Supporting Information is available from the Wiley Online Library or from the author.

Acknowledgements

Conflict of Interest

The authors declare no conflict of interest.

Keywords

[1] J.-S. Koh, E. Yang, G.-P. Jung, S.-P. Jung, J. H. Son, S.-I. Lee, P. G. Jablonski, R. J. Wood, H.-Y. Kim, K.-J. Cho, *Science* **2015**, *349*, 517.

[2] M. Wehner, R. L. Truby, D. J. Fitzgerald, B. Mosadegh, G. M. Whitesides, J. A. Lewis, R. J. Wood, *Nature* **2016**, *536*, 451.

[3] T. Li, G. Li, Y. Liang, T. Cheng, J. Dai, X. Yang, B. Liu, Z. Zeng, Z. Huang, Y. Luo, T. Xie, W. Yang, *Sci. Adv.* **2017**, *3*, e1602045.

[4] P. Nano EnergyFratzl, F. G. Barth, *Nature* **2009**, *462*, 442.

[5] O. M. Wani, H. Zeng, A. Priimagi, *Nat. Commun.* **2017**, *8*, 15546.

[6] M. A. McEvoy, N. Correll, *Science* **2015**, *347*, 1261689.

[7] S. J. Gershman, E. J. Horvitz, J. B. Tenenbaum, *Science* **2015**, *349*, 273.

[8] D. Rus, M. T. Tolley, *Nature* **2015**, *521*, 467.

[9] *Nat. Rev. Mater.* **2018**, *3*, 71.

[10] H. Zeng, P. Wasylczyk, D. S. Wiersma, A. Priimagi, *Adv. Mater.* **2018**, *30*, 1703554.

[11] L. Hines, K. Petersen, G. Z. Lum, M. Sitti, *Adv. Mater.* **2017**, *29*, 1603483.

[12] X.-Q. Wang, C. F. Tan, K. H. Chan, X. Lu, L. Zhu, S.-W. Kim, G. W. Ho, *Nat. Commun.* **2018**, *9*, 3438.

[13] J. Mu, G. Wang, H. Yan, H. Li, X. Wang, E. Gao, C. Hou, A. T. C. Pham, L. Wu, Q. Zhang, Y. Li, Z. Xu, Y. Guo, E. Reichmanis, H. Wang, M. Zhu, *Nat. Commun.* **2018**, *9*, 590.

[14] J. Mu, C. Hou, H. Wang, Y. Li, Q. Zhang, M. Zhu, *Sci. Adv.* **2015**, *1*, e1500533.

[15] W. Hu, G. Z. Lum, M. Mastrangeli, M. Sitti, *Nature* **2018**, *554*, 81.

[16] S. Bauer, S. Bauer-Gogonea, I. Graz, M. Kaltenbrunner, C. Keplinger, R. Schwödiauer, *Adv. Mater.* **2014**, *26*, 149.

[17] Y. Cheng, R. Wang, K. H. Chan, X. Lu, J. Sun, G. W. Ho, *ACS Nano* **2018**, *12*, 3898.

[18] H. Guo, X. Pu, J. Chen, Y. Meng, M.-H. Yeh, G. Liu, Q. Tang, B. Chen, D. Liu, S. Qi, C. Wu, C. Hu, J. Wang, Z. L. Wang, *Sci. Rob.* **2018**, *3*, eaat2516.

[19] K. Xu, Y. Lu, K. Takei, *Adv. Mater. Technol.* **2019**, *4*, 1800628.

[20] I. Graz, M. Krause, S. Bauer-Gogonea, S. Bauer, S. P. Lacour, B. Ploss, M. Zirkl, B. Stadlober, S. Wagner, *J. Appl. Phys.* **2009**, *106*, 034503.

[21] J. Hughes, U. Culha, F. Giardina, F. Guenther, A. Rosendo, F. Iida, *Front. Robot. AI* **2016**, *3*, 69.

[22] S. S. Robinson, K. W. O'Brien, H. Zhao, B. N. Peele, C. M. Larson, B. C. Mac Murray, I. M. Van Meerbeek, S. N. Dunham, R. F. Shepherd, *Extreme Mech. Lett.* **2015**, *5*, 47.

[23] C. Larson, B. Peele, S. Li, S. Robinson, M. Totaro, L. Beccai, B. Mazzolai, R. Shepherd, *Science* **2016**, *351*, 1071.

[24] H. Cheng, F. Zhao, J. Xue, G. Shi, L. Jiang, L. Qu, *ACS Nano* **2016**, *10*, 9529.

[25] M. Amjadi, M. Sitti, *Adv. Sci.* **2018**, *5*, 1800239.

[26] M. Kanik, S. Orguc, G. Varnavides, J. Kim, T. Benavides, D. Gonzalez, T. Akintilo, C. C. Tasan, A. P. Chandrakasan, Y. Fink, P. Anikeeva, *Science* **2019**, *365*, 145.

**ADVANCED
SCIENCE NEWS**

www.advancedsciencenews.com

**ADVANCED
MATERIALS**

www.advmat.de

[27] H. Yang, B. S. Yeow, Z. Li, K. Li, T.-H. Chang, L. Jing, Y. Li, J. S. Ho, H. Ren, P.-Y. Chen, *Sci. Rob.* **2019**, *4*, eaax7020.

[28] C. Wang, K. Sim, J. Chen, H. Kim, Z. Rao, Y. Li, W. Chen, J. Song, R. Verduzco, C. Yu, *Adv. Mater.* **2018**, *30*, 1706695.

[29] L. Chen, M. Weng, P. Zhou, F. Huang, C. Liu, S. Fan, W. Zhang, *Adv. Funct. Mater.* **2019**, *29*, 1806057.

[30] R. A. Bilodeau, E. L. White, R. K. Kramer, in *IEEE Int. Conf. on Intelligent Robots and Systems (IROS)*, IEEE, Piscataway, NJ, USA **2015**, pp. 2324–2329.

[31] H. Zhao, K. O'Brien, S. Li, R. F. Shepherd, *Sci. Rob.* **2016**, *1*, eaai7529.

[32] R. L. Truby, M. Wehner, A. K. Grosskopf, D. M. Vogt, S. G. M. Uzel, R. J. Wood, J. A. Lewis, *Adv. Mater.* **2018**, *30*, 1706383.

[33] X. Li, W. Xu, M. Tang, L. Zhou, B. Zhu, S. Zhu, J. Zhu, *Proc. Natl. Acad. Sci. USA* **2016**, *113*, 13953.

[34] C. R. Bowen, J. Taylor, E. LeBoulbar, D. Zabek, A. Chauhan, R. Vaish, *Energy Environ. Sci.* **2014**, *7*, 3836.

[35] S. Luo, T. Liu, *Adv. Mater.* **2013**, *25*, 5650.

[36] X.-Q. Wang, C. F. Tan, K. H. Chan, K. Xu, M. Hong, S.-W. Kim, G. W. Ho, *ACS Nano* **2017**, *11*, 10568.

[37] Y. Yang, W. Guo, K. C. Pradel, G. Zhu, Y. Zhou, Y. Zhang, Y. Hu, L. Lin, Z. L. Wang, *Nano Lett.* **2012**, *12*, 2833.

[38] J.-H. Lee, K. Y. Lee, M. K. Gupta, T. Y. Kim, D.-Y. Lee, J. Oh, C. Ryu, W. J. Yoo, C.-Y. Kang, S.-J. Yoon, J.-B. Yoo, S.-W. Kim, *Adv. Mater.* **2014**, *26*, 765.

[39] B. Shin, J. Ha, M. Lee, K. Park, G. H. Park, T. H. Choi, K.-J. Cho, H.-Y. Kim, *Sci. Rob.* **2018**, *3*, eaar2629.

[40] X. Ning, X. Yu, H. Wang, R. Sun, R. E. Corman, H. Li, C. M. Lee, Y. Xue, A. Chempakasseril, Y. Yao, Z. Zhang, H. Luan, Z. Wang, W. Xia, X. Feng, R. H. Ewoldt, Y. Huang, Y. Zhang, J. A. Rogers, *Sci. Adv.* **2018**, *4*, eaat8313.

[41] Y.-C. Cheng, H.-C. Lu, X. Lee, H. Zeng, A. Priimagi, *Adv. Mater.* **2020**, *32*, 1906233.

[42] A. Kotikian, C. McMahan, E. C. Davidson, J. M. Muhammad, R. D. Weeks, C. Daraio, J. A. Lewis, *Sci. Rob.* **2019**, *4*, eaax7044.

[43] A. Rafsanjani, Y. Zhang, B. Liu, S. M. Rubinstein, K. Bertoldi, *Sci. Rob.* **2018**, *3*, eaar7555.

[44] J. Kim, A. Banks, Z. Xie, S. Y. Heo, P. Gutruf, J. W. Lee, S. Xu, K.-I. Jang, F. Liu, G. Brown, J. Choi, J. H. Kim, X. Feng, Y. Huang, U. Paik, J. A. Rogers, *Adv. Funct. Mater.* **2015**, *25*, 4761.

2000351 (9 of 9)